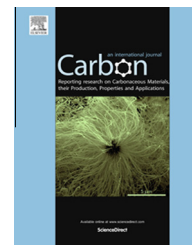


Available at [www.sciencedirect.com](http://www.sciencedirect.com)

ScienceDirect

journal homepage: [www.elsevier.com/locate/carbon](http://www.elsevier.com/locate/carbon)

# Nanocarbon aerogel complexes inspired by the leaf structure

Jing Zhong <sup>a,b,\*</sup>, Jing Meng <sup>c</sup>, Xuchun Gui <sup>d</sup>, Tao Hu <sup>e</sup>, Ning Xie <sup>c</sup>, Xiaoyan Lu <sup>a,b</sup>, Zhenyu Yang <sup>f</sup>, Nikhil Koratkar <sup>e,\*</sup>

<sup>a</sup> Key Lab of Structures Dynamic Behavior and Control (Harbin Institute of Technology), Ministry of Education, Harbin 150090, Heilongjiang, China

<sup>b</sup> School of Civil Engineering, Harbin Institute of Technology, Harbin 150090, China

<sup>c</sup> School of Transportation Science and Technology, Harbin Institute of Technology, Harbin 150090, China

<sup>d</sup> State Key Lab of Optoelectronic Materials and Technologies, School of Physics and Engineering, Sun Yat-sen University, Guangzhou 510275, China

<sup>e</sup> Department of Materials Science and Engineering, Rensselaer Polytechnic Institute, Troy, NY 12180, USA

<sup>f</sup> Department of Chemistry, Nanchang University, Nanchang 330031, China

## ARTICLE INFO

### Article history:

Received 20 February 2014

Accepted 23 May 2014

Available online 5 June 2014

## ABSTRACT

Inspired by the structure of a leaf, which is constituted of veins, midribs and laminae, we report the synthesis of aerogels based on nanocarbon complexes that exhibit good electrical conductivity, large internal surface area and stable structural integrity upon cyclic compression. These materials are prepared as monolithic solids from suspensions of unzipped and partially exfoliated multi-walled carbon nanotubes. Under optimized oxidation conditions, all the walls of the multi-walled carbon nanotubes are unzipped but only the outer tubes are exfoliated, creating nanoscale multi-layered graphene oxide sheets attached to inner trench-like structures. The exfoliated parts provide high surface area and functional groups, while the inner trench-like structures remain relatively intact and thus retain their electrical conductivity and mechanical properties, which facilitates charge transport and structural stability for the aerogel. The hydrophilic functional groups on the graphene oxide nanosheets make these structures highly soluble, and as a result, the density and mechanical properties can be adjusted to a large extent without sacrificing the porosity or cell wall uniformity. These nanocarbon aerogel complexes exhibit high damping capability with no significant change in piezoresistive properties after more than 4500 compressive cycles, and its original shape can be recovered quickly after compression release.

© 2014 Elsevier Ltd. All rights reserved.

## 1. Introduction

Carbon nanotube and graphene, combining extraordinary electrical, mechanical and thermal properties, are the most extensively explored carbon allotropes [1–5]. The ability to translate the unique properties of these nanoscale building

units into 3-D structures is a key step for a number of applications, especially in the areas of catalysis and energy conversion/storage which includes electrochemistry, photocatalysis as well as chemical and biological sensors [6–12]. Various methods, such as vacuum assisted filtration, self-gelation, hydrothermal, chemical vapour deposition (CVD) and ice

\* Corresponding authors.

E-mail addresses: [zhongjing.hit@gmail.com](mailto:zhongjing.hit@gmail.com) (J. Zhong), [koratn@rpi.edu](mailto:koratn@rpi.edu) (N. Koratkar).

<http://dx.doi.org/10.1016/j.carbon.2014.05.068>

0008-6223/© 2014 Elsevier Ltd. All rights reserved.

templating have been developed to fabricate nanocarbon based aerogels [13–18]. However, because of the competing requirements of high specific surface area and structural/mechanical/conductive properties (the former require nanocarbon building units exposed and separated as much as possible, while the latter require units piled up densely to enable effective stress/mass transfer), most of the existing porous carbon aerogels display either low surface area or poor structural integrity and elasticity. For example, carbon nanotubes aerogels in the form of forests and sponges, possess characteristics of high electrical conductivity and superelasticity resulting from their tubular or fibrillar structure with high bending stiffness, however, their application in the energy-related area is limited by their relatively low specific surface area [19–23]. By contrast, graphene oxide or reduced graphene oxide based aerogels offer higher specific surface area but their electrical conductivity is inadequate due to irreversible chemical oxidation of graphene oxide [24–28]. In addition, a homogenous and stable graphene oxide dispersion with high concentration ( $>10$  mg/ml) is difficult to achieve, mainly due to the 2-D characteristics of the graphene oxide nanosheets [26]. Organic functionalization is also a strategy that has been used to manipulate the nanocarbon building blocks [27–29]. Grafted with organogelators, these building blocks can be cross-linked and result in highly porous interconnected structures [29]. However, it should be noted that the functionalization process would unavoidably induce some agglomeration, which results in non-uniform structures of the cell walls. From the above discussion it is evident that simultaneous realization of mechanical strength and electrical conductivity without sacrificing high specific surface area is challenging to achieve.

To design an appropriate structure that can possess all the above mentioned properties, we examined a variety of existing natural structures. As one of the most ubiquitous natural structures, trees and leaves (Fig. 1) are particularly interesting. They stand up to strong winds and rains (good mechanical properties), meanwhile absorb nutrients and water through veins and midribs from roots (stable mass transportation highway), and sunlight via laminas for photosynthesis (high surface area). It is the veins and midribs that are responsible for structural stability and mass transportation, whereas laminas provide more surfaces which facilitate photon absorption. Such multifunctionality exhibited by natural structures inspired us to synthesize leaf-like aerogels based on nanocarbon complexes. Recently, the synthesis and applications of unzipped carbon nanotubes have attracted considerable attention, due to their unique physical and chemical properties. Since Tour reported the oxidation unzipping method to successfully realize the high yield of unzipped CNT (UCNT) with low cost in 2009 [30,31], the application of UCNT in various areas, including fabrication of composites with enhanced mechanical properties, energy conversion and storage, as well as water purification, have been intensely explored [32–37]. Thanks to the rapid advances in graphene science in recent years, various synthesis strategies for graphene can be adapted to produce UCNT based advanced materials that take advantage of the unique nanoribbon structure of UCNT. In this study, we unzipped multi-walled carbon nanotubes (MWCNT) with optimized oxidation condition, creating

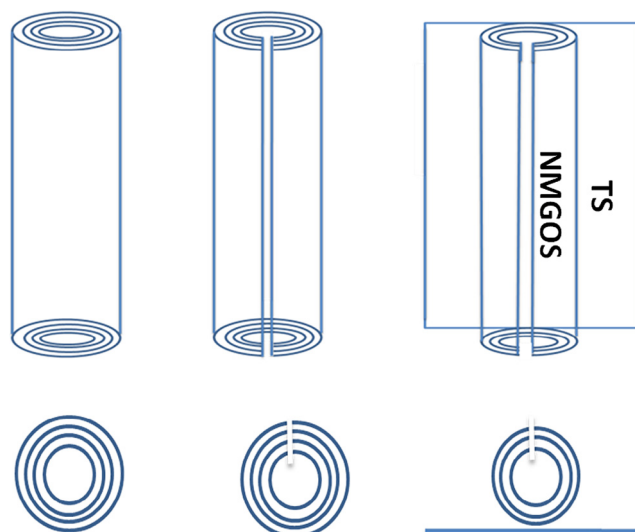


**Fig. 1 – Schematic illustration of leaf-inspired nanocarbon aerogel complexes. (A colour version of this figure can be viewed online.)**

nanoscale multi-layered graphene oxide sheets (NMGOS) attached to the unzipped but un-exfoliated inner tubes which form a trench-like structure (TS) (Fig. 1). These NMGOS-TS nanocarbon complexes are highly soluble in water, and thus can be freeze-dried to aerogels with controllable density and mechanical properties. Within this aerogel, the NMGOS provide high specific surface area, playing the similar role as laminas in leaves, whereas the relatively intact TS with good mechanical and conductive properties provide a structurally stable highway for electron transportation, mimicking the functionalities of veins and midribs in leaves.

## 2. Experimental

MWCNTs prepared by chemical vapour deposition were purchased from TIMENANO ( $>95\%$  purity; outer diameter  $> 50$  nm; inner diameter 5–15 nm, 20–30 walls). Nanocarbon complex was prepared using a modified Hummers' method. MWCNTs (1.5 g) were dispersed in 360 ml concentrated  $H_2SO_4$  in a flask by stirring the mixture continuously for 1 h, followed by the addition of 40 ml  $H_3PO_4$  (85%).  $KMnO_4$  (1.5, 3, 4.5, 6, 7.5 g, and the unzipped CNTs are termed as UCNT\_1 to UCNT\_5) was added to the mixture slowly. The mixture is then heated to  $65^\circ C$  for another 1 h before poured onto 1000 ml of ice containing 50 ml  $H_2O_2$  (30%). The dispersion was centrifuged at 9500 r.p.m for 0.5 h to collect solid, which was then washed by HCl, ethanol and ether successively. The collected solid was vacuum dried. To prepare UCNT aerogel, the UCNT was firstly dispersed in DDI water (Millipore water with a resistant of 18 M $\Omega$ ) by tip sonication for 30 min with a power of 300 W, and then the dispersion is unidirectionally frozen by letting the bottom of the dispersion container contact with liquid nitrogen, and aerogels can be eventually obtained after sublimation. The aerogels were further annealed at  $200^\circ C$  for 2 h to reduce the aerogels upon partially eliminating oxygen functional groups. The structures of the aerogels were investigated by scanning electron

microscopy (HELIOS Nanolab 600i). TEM images were collected on a Tecnai G2 F30 system. Surface areas were measured by 3H-2000BET-A (BeiShiDe Instrument). X-ray diffraction (XRD, Empyrean series2, PANalytical) and Raman spectrum (LabRAM HR Evolution) were also collected to analyze the structure of UCNT. In order to qualitatively check the oxidation and reduction degree, thermal gravimetric analysis (TGA, EXSTAR TG/DTA7000) was performed with a heating rate of 10 °C from room temperature to 1000 °C under the N<sub>2</sub> gas protection. The mechanical properties of aerogels were test by Instron 8628 with a load cell of 2 N. The piezoresistance properties were tested in a strain range of 20–50% in a model of cyclic compression, and the electrical conductivity was measured and monitored by using the two electrodes method as shown in Fig. S3.

### 3. Results and discussion

For the preparation of nanocarbon complexes, MWCNTs were oxidized in KMnO<sub>4</sub>/H<sub>2</sub>SO<sub>4</sub> dispersion at 65 °C by systematically varying the concentration of KMnO<sub>4</sub> from mild to harsh oxidation condition (KMnO<sub>4</sub>:MWCNT mass ratio from 1 to 5, thus named as UCNT\_1 to UCNT\_5, which represents the degree of oxidation), as reported by Tour's group [30,31]. Dispersions with concentration as high as 100 mg/ml, can be stable without any noticeable sedimentation after 3 weeks. Such super solubility is mainly resulted from their hierarchical structure. The nanocarbon complexes are comprised of hydrophobic TS and hydrophilic NMGOS, behaving in a manner akin to a surfactant-coated particle, and thus are not only kinetically but also thermodynamically stable. Figs. 2a–c and S1 present transmission electron microscopy (TEM) images of the pristine MWCNT and UCNT materials. Clearly, the unzipping process is initiated from the outermost layer, and more layers are unzipped with increasing amount of KMnO<sub>4</sub>. At low mass ratio of KMnO<sub>4</sub>/MCNT (MR < 3), only the outer tubes are successfully unzipped, while the inner tubes are intact. As the MR increased to 3 (UCNT\_3), almost all the tubes, from the outermost to innermost one, are fully unzipped, since the width of the channel (>30 nm) formed by the UCNT is much larger than the inner diameter (~10 nm) of the pristine CNT. Note that in this study, we report much higher cutting efficiency of our CNT than the one previously reported by Tour [30,31]. Considering the similar CNT diameter and wall thickness in this study with that used by Tour (description of CNT used in Tour's report: outer diameter 40–80 nm, inner diameter 5–15 nm, 20–30 walls) [30,31], such different unzipping kinetics are probably resulted from the inferior quality of the CNT employed in this study as evidenced by Raman spectroscopy analysis provided later in this article. It was found that all of the unzipped CNT present straight and even edges, and more specifically, the outer tubes are not only unzipped, but also exfoliated and create thin edges to form NMGOS, while the inner tubes are only unzipped but not exfoliated thus forming TS with relatively thick edges (Fig. 2c). Further increasing the MR (UCNT\_4) can still enhance the extent of exfoliation of the outer tubes, but the TS seems not sensitive to the further addition of KMnO<sub>4</sub>. As can be seen from Fig. S1d for UCNT\_5, the

NMGOSs originated from different MWCNT are large enough to overlap, while the TSs are evenly distributed. X-ray photoelectron spectroscopy (XPS) results (Fig. 2d) reveal that increasing the dosage of oxidant enhances the amount of hydrophilic functional groups on the surface of the nanocarbon complexes, most of which can be subsequently removed by thermal reduction in spite of the relatively mild reduction conditions employed in this study. The effectiveness of such reduction methods is also confirmed by the TGA results shown in Fig. S6. The structures of the CNT before and after unzipping treatment are investigated by XRD and Raman spectroscopy, as shown in Figs. S7 and S8. The inter-layer spacing varies with increasing oxidation degree and eventually a peak at ~10.8° is created which corresponds to a spacing of ~0.82 nm. These XRD results are very similar to that of graphite oxide and unzipped CNT reported by Tour [30]. The high D peak intensity of CNT shown in the Raman spectroscopy results indicates the defective characteristic of our CNT, which is probably the reason for the different unzipping kinetics of our CNT comparing to Tour's. The D-peak intensity of the CNT after the oxidation and reduction process is almost the same. The D:G ratios of CNT, UCNT and reduced UCNT (RUCNT) are 1.13, 1.46 and 1.53, respectively. Such count-intuitive phenomenon of increasing of this ratio after reduction is also observed in Tour's report [30,31]. The structural evolution of MWCNT by the unzipping process was also investigated by BET analysis as shown in Fig. 2e. A pore size peak at 3.5 nm emerged when the MR is higher than 2 (UCNT\_3, UCNT\_4 and UCNT\_5). The origin of these pores is not clear at this point, but it is likely that this resulted from the partially exfoliated parts of UCNT. The specific surface area of UCNT linearly increase with its degree of oxidation, and is tripled when the MR reach 5, from ~102 to ~302 m<sup>2</sup>/g (Fig. 2f). Note that the pristine MWCNT employed here has more than 20 tubes with a relatively small specific surface area; therefore even greater specific surface areas could possibly be achieved by using MWCNT with fewer tubes and walls. Another interesting observation is that the process for the formation of NMGOS-TS structure does not follow the pattern as described by Tour, in which the MWCNT is stepwisely unzipped to form nanoribbons [30,31]. Instead, for our MWCNT, it appears that the exfoliation and formation of nanoribbons is initiated only when the whole MWCNT is fully unzipped. This is presumably caused by the highly defective characteristic of our MWCNT. From the above analysis of XRD and Raman data, we conjectured that the unzipping process and the unzipping degree are controlled by the degree of defects, such as grain boundaries and the content of sp<sup>3</sup> hybridized carbon atoms but not the degree of crystallization. When the MWCNTs are successfully unzipped, they can be exfoliated by sonication, similar to the process for graphene oxide synthesis from graphite oxide. As the oxidation intensified (MR > 3), more functional groups can be attached to the galleries of MWCNT, which increase the inter-planer distance of UCNT and facilitates their full exfoliation from TS under aggressive tip sonication. It can be seen from Fig. S1e that the trench-like structures can still be distinguished even when the MR is as high as 10, yet with much smaller diameters. Such observation supports the above proposed exfoliation mechanism.

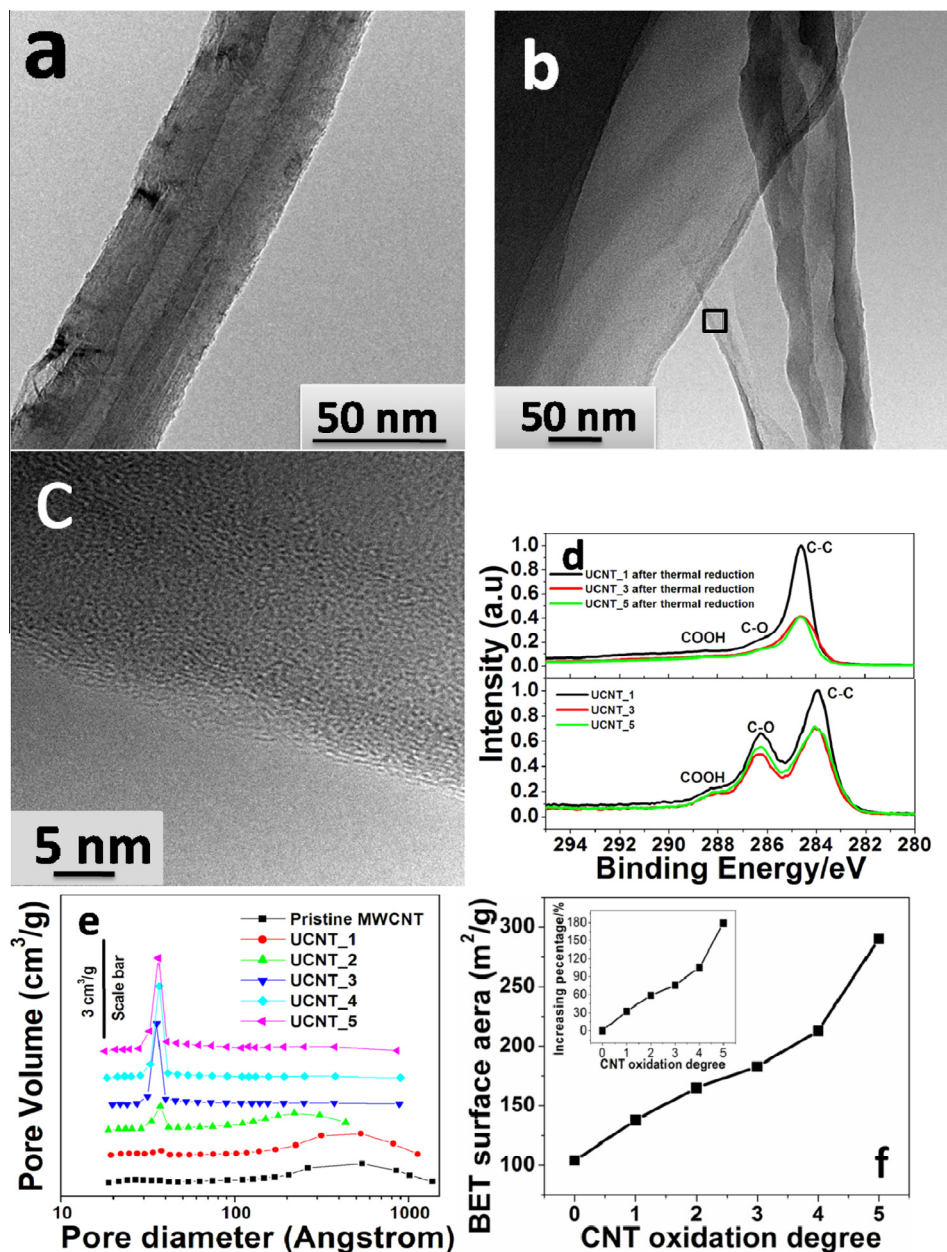


**Fig. 2** – Structural characterization of UCNT. (a) TEM image of pristine MWCNT. (b) TEM image of UCNT<sub>4</sub>. (c) TEM image of the box in (b) with high magnification. (d) XPS results showing the chemical structures of UCNT before and after thermal reduction at 200 °C for 2 h. (e) Pore size distribution of unzipped CNT with different oxidation degree. (f) BET surface areas indicating a large increase with the oxidation degree of the UCNT. Inset image shows the surface area increasing percentage with the oxidation degree. (A colour version of this figure can be viewed online.)

Next, we take advantage of a versatile, highly efficient solution phase shaping technique, namely ice templating, to investigate the possibility of assembling these nanocarbon complexes into leaf-like aerogels. It is well known that redistribution of nanoparticles occurs during the crystallization of liquid, which is induced by the rejection of nanoparticles due to ice formation [38–40]. Highly porous aerogels can be obtained via subsequent sublimation. Such ice-segregation induced self assembly process (ISISA) has been successfully adopted for the preparation of materials with highly sophisticated structures, including polymeric, ceramic, metallic and composite materials [40–42]. In this study, the nanocarbon

dispersions were unidirectionally frozen by letting the bottom of the dispersion container contact with liquid nitrogen (Fig. 3a, bottom), and subsequent sublimation results in highly porous and self-supported aerogels with a tree-branch structure in the form of sheets connected by primary venations (arrows in Fig. 3b–d) running through almost the whole sample without any break and arranged in a parallel fashion in the vertical direction (direction of freezing and temperature gradient), as shown in Fig. 3b–d. As can be seen from the higher amplification SEM images shown in Fig. 3(e–f), the sheets are piled up, with NMGOs from different UCNT contacting each other and TSs providing structural stability,

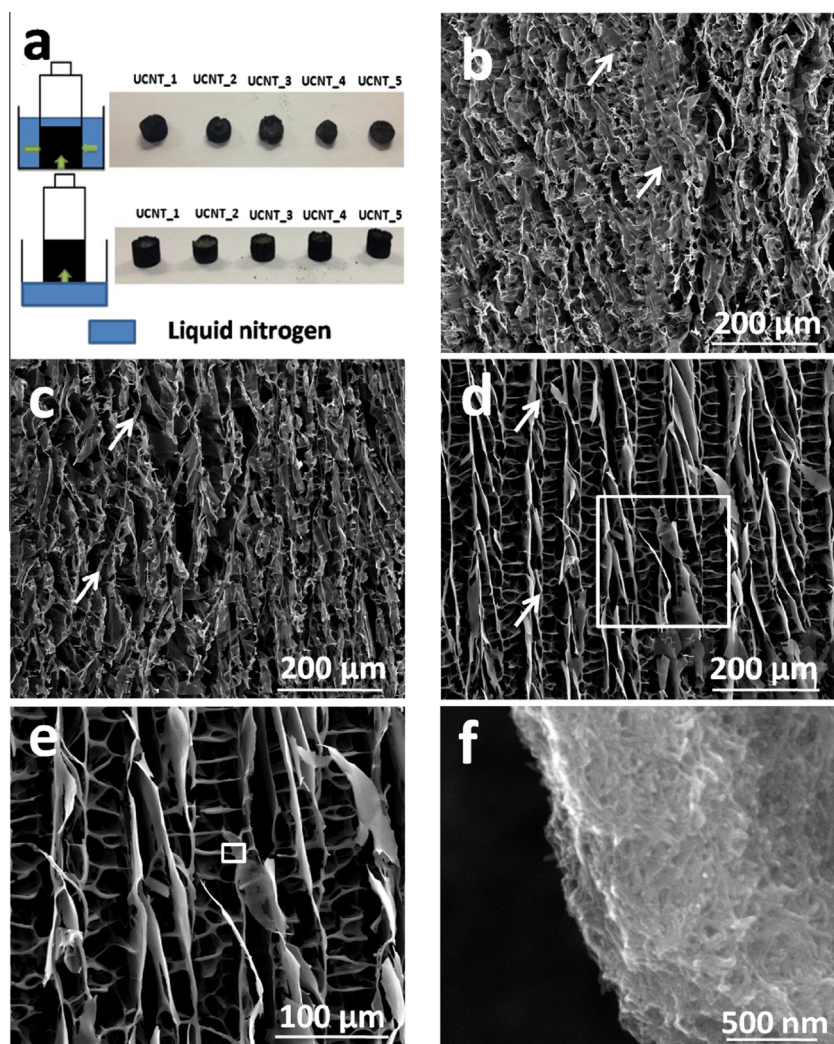


**Fig. 3** – ISISA process comparison and SEM images of nanocarbon complexes aerogels, showing the evolution of Pores and cell walls structure with increasing the oxidation degree (with concentration of 20 mg/ml). (a) Schematic of random ice template (upper) and unidirectional ice template (bottom). (b) UCNT\_1. (c) UCNT\_3. (d) UCNT\_5. (e) Enlarged image of the box in (d). (f) Enlarged image of the box in (e). (A colour version of this figure can be viewed online.)

similar to the structure of leaves. Note that, the morphology of the resulting architecture is dependent on the oxidation degree of MWCNT; that is, increasing the oxidation degree favors regularity in the structures, as well as enhancement of the cell wall thickness. The UCNT\_5 aerogel shown in Fig. 3(d–f), clearly illustrate that the primary venations and leaf-like sheets are perfectly aligned in the vertical and horizontal directions, respectively, generating honeycomb structures. Such leaf-like structures are resulted not only from the unique structure of the nanocarbon complex, but also the unidirectional freezing methodology. Indeed upon random freezing-dry, the pores and walls of the resulted monoliths are randomly distributed without any cell wall alignment and honeycomb structures (Figs. 3a and S2). The high dispersibility of nanocarbon complexes allows us to fabricate aerogels with various densities and thus adjust their mechanical and electrical properties. Various concentrations (from 5 to 30 mg/ml) of homogeneous aqueous suspensions of nanocarbon complexes with different oxidation degrees

(from UCNT\_1 to UCNT\_5) were used to fabricate aerogels. Increasing the concentration of nanocarbon complexes can enhance the continuity and thickness of the cell walls, which increases the density, and in turn improves the mechanical and electrical properties of the aerogels, as shown in Figs. 4 and 5. Besides ISISA method, the other two common aerogel/hydrogel preparation methods, namely, hydrothermal and self-assembly by chemical reduction followed by freeze-drying, were also explored to investigate the effects of the preparation method on the aerogel structures. However, both these methods resulted in highly brittle monoliths with randomly distributed pores and walls structures (no honeycomb structures were observed in these cases: see Figs. S4 and S5). Therefore, only the aerogels fabricated by the ISISA method were further tested.

Compression tests (Fig. 4) revealed that the nanocarbon complex aerogels exhibited excellent resilience and hysteresis damping properties. Our aerogel can bear a compression strain as high as 80% and recover original shape with

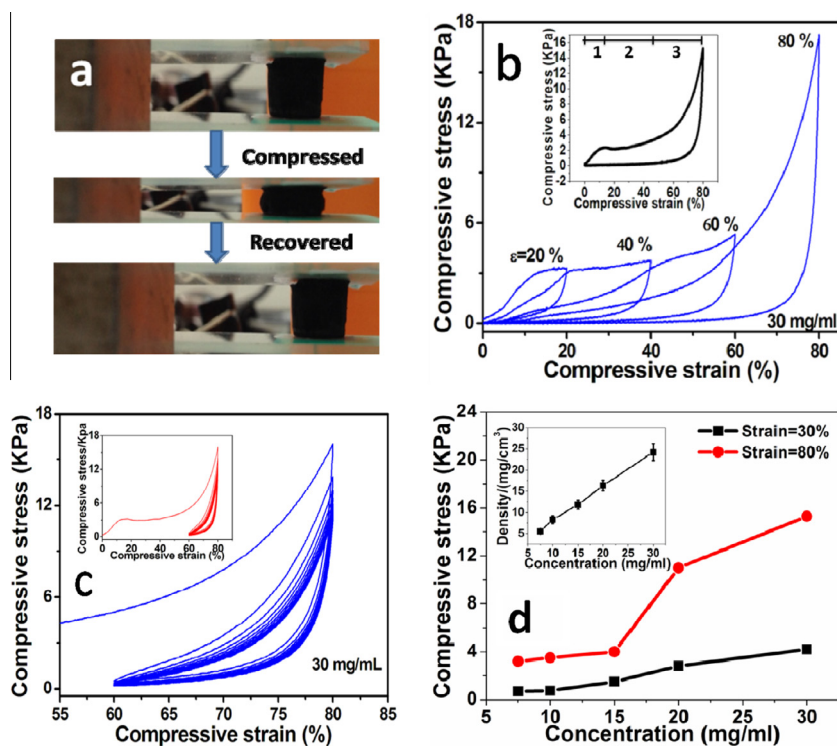


**Fig. 4** – Mechanical properties of UCNT aerogels. (The strain rate is 20%/min). (a) Photos demonstrating the resilience of the nanocarbon aerogel complexes. (b) Compression tests in a mode of successively increasing maximum strain (aerogel from UNCT\_4). Inset image shows a typical aerogel compression curve, in which the three compression stages are indicated. (c) Cyclic compression in a strain range of 60–80% (aerogel from UNCT\_4). Inset image shows the whole compression process. (d) Concentration dependence of compressive stress. Inset image shows the concentration dependence on density of the aerogel. (A colour version of this figure can be viewed online.)

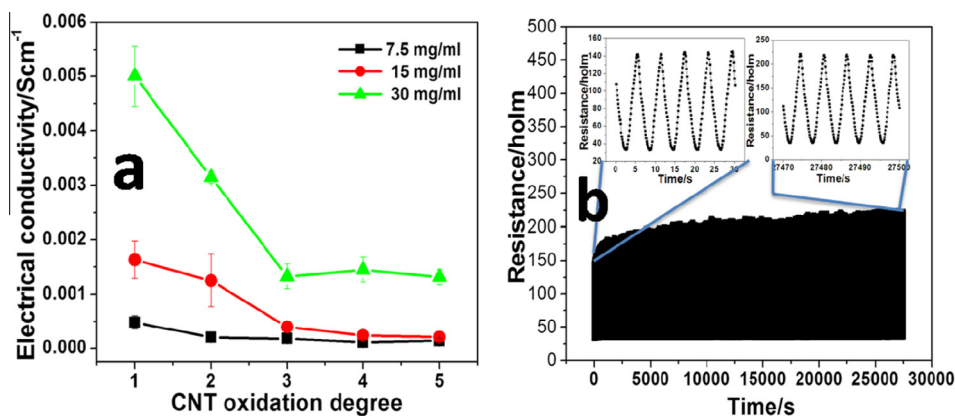


**Fig. 5** – Stable electrical conductivity properties upon cyclic compression (aerogel from UCNT\_4). (a) Electrical conductivity dependence on oxidation degree and dispersion concentration of UCNT. (b) Piezoresistive property of aerogel for >4500 cycles upon compression in the strain range of 20–50% in a sinusoidal cyclic compression mode with a frequency of 10 rad/s. (A colour version of this figure can be viewed online.)

marginal residual strain (Inset in Fig. 4b). The strain is the ratio between the compression distance and the initial height of aerogel. Three stages of deformation can be observed in the loading stress–strain curve, which are typical behaviors of porous monoliths, namely, a linear elastic region resulting from the bending of the aerogel walls (stage 1); relatively flat stress plateau resulting from the elastic buckling of the walls (stage 2) and followed by an abrupt stress rise corresponding

to the densification of the cell walls (stage 3) [43,44]. To explore the evolution of mechanical properties under loading–unloading cycles, we tested our aerogels by progressively increasing the maximum strains (from 20% to 80%). As shown in Fig. 4(b), when the maximum strains increased in the successive compressive loading–unloading cycles, the Young's modulus declined, accompanied by expansion of the linear elastic regions. The stress plateau region firstly expands and

then shrinks; the region with an abrupt increase in stress emerges when the maximum strain exceeds  $\sim 60\%$ . Such an evolution of mechanical properties reflects changes to the structure of the network upon compression cycling. Indeed, during the compression with relatively low strain ( $<60\%$ ), once stable nodes are formed through structural rearrangement of cell walls, the aerogel can undergo large effective compression strain just by rotations about such nodes without inducing significant stress in the solid material itself. Therefore, the aerogels show lower resistive stress and Young's modulus in the following compression cycles. Fig. 4d presents the dependence of the stress (corresponding to the maximum strains) and the aerogel density (inset) on the concentration of the UNCT dispersion. At the low maximum strain (30%), the stress increases almost linearly with concentration, while for the high maximum strain (80%), the stress increases abruptly at a concentration of  $\sim 20$  mg/ml. Such an abrupt rise can be attributed to cell wall densification, which is influenced by both the UNCT concentration and the applied strain. The area enclosed by the loading–unloading curve is a signature for the damping properties of aerogels, and this indicates that our aerogel possesses excellent energy dissipation capability. Such super resilience combined with high damping capability is similar to the behavior of viscoelastic polymer materials. For aerogels or foams, two energy-loss mechanisms could possibly explain the damping during compression cycles: (1) structural damping because of snapping events, such as kinking or local sliding of UCNT. (2) Friction between adjacent cell walls [45,46]. Since the emergence of stage 3 marks the occurrence of densification of cell walls [43,44], it is reasonable to conjecture that the friction between cell walls in this stage should be much more severe than the previous stages. Thus, we designed a loading–unloading procedure to specifically test the mechanical behaviors of stage 3 to further seek the mechanism of damping for our aerogel: the aerogel was firstly compressed to the strain of 80% followed by unloading to the strain of 60%, and then we performed cyclical loading–unloading in the strain range of 60–80% (Inset in Fig. 4c). As can be seen from Fig. 4c, the cycling curves are almost overlapping with small hysteresis loops, from which we conclude that the friction between cell walls during densification is negligible for energy dissipation and the damping from snapping should be the dominant factor for energy dissipation. Therefore, to enhance the damping performance of aerogel, the structures and morphologies of the cell walls but not the pores structures should be focused on.

The unique structure of the aerogel also gives rise to superior electrical conductivity. The honeycomb structure of our aerogel with the presence of the primary venations (leaf-like sheet structure), ensures stable pathways for electron transportation as well as mechanical stability. Indeed, the electrical conductivity of our UCNT\_1 aerogel with a density of  $\sim 5$  mg/cm<sup>3</sup> was measured to be 0.005 S/cm, which is one order higher than graphene aerogels fabricated via hydrothermal method, and three orders higher than polyvinyl alcohol reinforced carbon nanotube aerogels [47,48]. The fatigue piezoresistance testing process for aerogels (upon 4500 loading/unloading cycles, in the strain range of  $20\% < \epsilon < 50\%$ , in a sinusoidal displacement mode with a frequency of

10 rad/s) can be seen in the video in the [Supplementary Materials](#), and the testing results can be seen in Fig. 5a and b. The response of the electrical conductivity of the aerogel is fairly constant after the first 1000 cycles with maximum resistance increase of only  $\sim 0.5\%$  per cycle. The maximum electrical resistance increases gradually from  $\sim 160$  to  $\sim 210 \Omega$  over 4500 cycles. As can be seen from Fig. S9, the microstructural change of the aerogels after 4500 cycles is not significant. Such stable piezoresistive performance under cyclic compression is remarkable for aerogels, and this is again resulted from the unique morphology of our bio-inspired honeycomb structure formed by leaf-like sheets.

#### 4. Conclusions

In summary, we have developed macroscopic, multi-functional, bio-inspired honeycomb aerogels with a leaf-like structure, by combining the unidirectional ice template method with NMGOS-TS nanocarbon complexes as building blocks. The nanocarbon complexes are formed by oxidation method, which unzip the whole MWCNT but only exfoliate the outer MWCNT tubes. The combination of the NMGOS with TS results in a unique hierarchical structure for the nanocarbon complex, which not only endows the aerogels with large specific surface area ( $>300$  m<sup>2</sup>/g), but also high mechanical damping and stable electrical properties upon compression. These desirable multifunctional attributes could enable many applications, such as piezoresistance devices, supercapacitors and catalyst substrates.

#### Appendix A. Supplementary data

Supplementary data associated with this article can be found, in the online version, at <http://dx.doi.org/10.1016/j.carbon.2014.05.068>.

#### REFERENCES

- [1] Geim AK, Novoselov KS. The rise of graphene. *Nat Mater* 2007;6:183–91.
- [2] Stankovic S, Dikin DA, Dommett GHB, Kohlhaas KM, Zimney EJ, Stach EA, et al. Graphene-based composite materials. *Nature* 2006;442:282–6.
- [3] Baughman RH, Zakhidov AA, De Heer WA. Carbon nanotubes—the route toward application. *Science* 2002;297:787–92.
- [4] Huang X, Qi X, Boey F, Zhang H. Graphene based composites. *Chem Soc Rev* 2012;41:666–86.
- [5] He Q, Wu S, Yin Z, Zhang H. Graphene based electronic sensors. *Chem Sci* 2012;3:1764–72.
- [6] Huang X, Ying Z, Wu S, Qi X, He Q, Zhang Q, et al. Graphene based materials: synthesis, characterization, properties, and applications. *Small* 2011;7:1876–902.
- [7] Cao X, Yin Z, Zhang H. Three dimensional graphene materials: preparation, structures and application in supercapacitors. *Energy Environ Sci* 2014;7:C4EE00050A.
- [8] Cao X, Zheng B, Rui X, Shi W, Yan Q, Zhang H. Metal oxide coated three dimensional graphene prepared by the use of metal organic frameworks as precursors. *Angew Chem Int Ed* 2014;53:1404–9.

- [9] Cao X, Shi Y, Shi Y, Shi X, Rui X, Zhang H. Preparation of MoS<sub>2</sub> coated three dimensional graphene networks for high performance anode material in lithium ion batteries. *Small* 2013;9: 3433–3428.
- [10] Cao X, Zeng Z, Shi W, Yep P, Yan Q, Zhang H. Three dimensional graphene network composites for detection of hydrogen peroxide. *Small* 2013;9:1703–7.
- [11] Cao X, Shi Y, Shi W, Lu G, Huang X, Yan Q, et al. Preparation of novel 3D graphene network for supercapacitor application. *Small* 2011;7:3163–8.
- [12] Vigolo B, Penicaud A, Coulon C, Sauder C, Pailler R, Journet C. Macroscopic fibers and ribbons of oriented carbon nanotubes. *Science* 2000;290:1331–4.
- [13] Yang X, Cheng C, Wang Y, Qiu L, Li D. Liquid-mediated dense integration of ... for compact capacitive energy storage. *Science* 2013;341:534–7.
- [14] Zhao Y, Hu C, Hu Y, Cheng H, Shi G, Qu L, et al. Ultralight, nitrogen-doped graphene framework. *Angew Chem* 2012;124:11533–7.
- [15] Xu Y, Sheng K, Li C, Shi G. Self-assembled graphene hydrogel via a one-step hydrothermal process. *ACS Nano* 2010;4:4324–30.
- [16] Bai H, Li C, Wang X, Shi G. On the gelation of graphene oxide. *J Phys Chem C* 2011;115:5545–51.
- [17] Reddy ALM, Shaijumon MM, Gowda SR, Ajayan PM. Coaxial MnO<sub>2</sub>/carbon nanotube array electrodes for high-performance lithium batteries. *Nano Lett* 2009;9:1002–6.
- [18] Hu L, Choi JW, Yang Y, Jeong S, Mantia FL, Cui L, et al. Highly conductive paper for energy-storage devices. *PNAS* 2009;107:3:1–5.
- [19] Hough LA, Islam MF, Janmey PA, Yodh AG. Viscoelasticity of single wall carbon nanotube suspensions. *Phys Rev Lett* 2004;93:168102.
- [20] Bi H, Huang X, Wu X, Cao X, Tan C, Yin Z, et al. Carbon microbelt aerogel prepared by waste paper: an efficient and recyclable sorbent for oils and organic solvents. *Small* 2014;201303413.
- [21] Bi H, Yin Y, Cao X, Xie X, Tan C, Huang X, et al. Carbon fiber aerogel made from raw cotton: a novel, efficient and recyclable sorbent for oils and organic solvents. *Adv Mater* 2013;25:5916–21.
- [22] Gui X, Wei J, Wang K, Cao A, Zhu H, Jia Y, et al. Carbon nanotube sponges. *Adv Mater* 2010;22:617–21.
- [23] Gui X, Cao A, Wei J, Li H, Jia Y, Li Z, et al. Soft, highly conductive nanotube sponges and composites with controlled compressibility. *ACS Nano* 2010;4:2320–6.
- [24] Xu Y, Lin Z, Huang X, Liu Y, Huang Y, Duan X. Flexible solid-state supercapacitors based on three-dimensional graphene hydrogel films. *ACS Nano* 2013;7:4042–9.
- [25] Zhu Y, Murali S, Cai W, Li X, Suk JW, Potts JR, et al. Graphene and graphene oxide synthesis properties and application. *Adv Mater* 2010;22:3906–24.
- [26] Qiu L, Liu Z, Chang S, Wu Y, Li D. Biomimetic superelastic graphene-based cellular monoliths. *Nat Commun* 2012;3:1241–6.
- [27] Kim KH, Oh Y, Islam MF. Graphene coating makes carbon nanotube aerogels superelastic and resistant to fatigue. *Nat Nanotechnol* 2012;7:562–6.
- [28] Sudeep PM, Narayanan TN, Ganesan A, Shaijumon MM, Yang H, Ozden S, et al. Covalently interconnected three-dimensional graphene oxide solid. *ACS Nano* 2013;7:7034–40.
- [29] Sun H, Xu Z, Gao C. Multifunctional, ultra-flyweight, synergistically assembled carbon aerogels. *Adv Mater* 2013;25:2554–60.
- [30] Kosynkin DV, Higginbotham AL, Sinitskii A, Lomeda JR, Dimiev A, Katherine B, et al. Longitudinal unzipping of carbon nanotubes to form graphene nanoribbons. *Nature* 2009;458:872–7.
- [31] Higginbotham AL, Kosynkin DV, Sinitskii A, Sun Z, Tour JM. Low-defect graphene oxide nanoribbons from multiwalled carbon nanotubes. *ACS Nano* 2010;4:2059–69.
- [32] Lin J, Raji AR, Nan K, Peng Z, Yan Z, Samuel ELG, et al. Iron oxide nanoparticle and graphene nanoribbon composite as an anode material for high-performance li-ion batteries. *Adv Funct Mater* 2013;24:2044–8.
- [33] Lin J, Peng P, Xiang C, Ruan G, Yan Z, Natelson D, et al. Graphene nanoribbon and nanostructured SnO<sub>2</sub> composite anodes for lithium ion batteries. *ACS Nano* 2013;7:6001–6.
- [34] Rafiee MA, Lu W, Thomas AV, Zandiatashbar A, Rafiee J, Tour JM, et al. Graphene nanoribbon composites. *ACS Nano* 2010;4:7415–20.
- [35] Xiang X, Young CC, Wang X, Yan Z, Hwang CC, Ceriotti G, et al. Large flake graphene oxide fiber with unconventional 100% knot efficiency and highly aligned small flake graphene oxide fiber. *Adv Mater* 2013;25:4592–7.
- [36] Carretero-Gonzalez J, Castillo-Martinez E, Lima MD, Acik M, Rogers DM, Sovich J, et al. Oriented graphene nanoribbon yarn and sheet from aligned multi-walled carbon nanotube sheets. *Adv Mater* 2012;24:5695–701.
- [37] Peng Q, Li Y, He X, Gui X, Shang Y, Wang C, et al. Graphene nanoribbon aerogels unzipped from carbon nanotube sponges. *Adv Mater* 2014;3.
- [38] Deville S. Freeze-casting of porous ceramics. *Adv Eng Mater* 2008;10:155–69.
- [39] Butler MF. Growth of solutal ice dendrites studied by optical interferometry. *Cryst Growth Des* 2002;2:59–66.
- [40] Deville S, Saiz E, Nalla RK, Tomsia AP. Freezing as a path to build complex composites. *Science* 2006;311:515–8.
- [41] Lau C, Cooney MJ, Atanassov P. Conductive macroporous composite chitosan–carbon nanotube scaffolds. *Langmuir* 2008;24:7004–10.
- [42] Bouville F, Maire E, Meille S, Moortele BVD, Stevenson AJ, Deville S. Strong, tough and stiff bioinspired ceramics from brittle constituents. *Nat Mater* 2014;13:508–14.
- [43] Liang H, Guan Q, Chen L, Zhu Z, Zhang W, Yu S. Macroscopic-scale template synthesis of robust carbonaceous nanofiber hydrogels and aerogels and their applications. *Angew Chem Int Ed* 2012;51:5101–5.
- [44] Schaedler TA, Jacobsen AJ, Torrents A, Sorensen AE, Lian J, Greer JR, et al. Ultralight metallic microlattices. *Science* 2011;334:962–5.
- [45] Ashby MF, Mehl Medalist RF. The mechanical properties of cellular solids. *Metall Trans A* 1983;14:1755–69.
- [46] Yang Y, Gupta MC, Dudley KL, Lawrence RW. Conductive carbon nanofiber-polymer foam structure. *Adv Mater* 2005;17:1999–2003.
- [47] Tang Z, Shen S, Zhuang J, Wang X. Noble-metal-promoted three-dimensional macroassembly of single-layered graphene oxide. *Angew Chem* 2010;49:4603–7.
- [48] Bryning MB, Milkie DE, Islam MF, Hough LA, Kikkawa JM, Yodh AG. Carbon nanotube aerogels. *Adv Mater* 2007;17:661–4.